ORIGINAL RESEARCH

Cellulose as a polyol in the synthesis of bio-based polyurethanes with simultaneous film formation

Deyvid S. Porto · Ana Cassales · Heloisa Ciol · Natalia M. Inada · Elisabete Frollini

Abstract Despite the wide availability of cellulose, this polyhydroxylated polysaccharide has practically not been used in the synthesis of polyurethanes (PUs), a family of polymers with great versatility. Microcrystalline cellulose (MCC) was used as a polyol to synthesize PUs, mostly at room temperature, with no solvent or catalyst, and simultaneous film formation. Castor oil (CO) was used as an additional polyol and MCC dispersant in the reaction medium. 0–60% of MCC was used regarding the concentration of hydroxyl groups in CO. FTIR spectroscopy indicated that all of the isocyanate groups reacted. The films were extensively characterized; in short, they exhibit transparency, high crystallinity (~75%; scanning electron microscopy and polarized light microscopy suggest the formation of spherulite), intermediate hydrophobicity (contact angle > 85°). Considering the control film (100% CO as polyol) and the film prepared using 60% MCC, T_g ranged from sub-ambient (9 °C) to 78 °C, tensile strength from 0.2 to 14 MPa, Young's modulus from 2 to 474 MPa, and elongation from 21 to 13% (the film prepared using 45% MCC showed 102%). The results from ultraviolet–visible spectroscopy, thermogravimetry, and swelling tests are also shown. The properties of the films formed during the reaction performed at 100 °C (using 60% MCC) were discussed. Biocompatibility tests showed cell viability above 90% after 168 h, indicating noncytotoxicity for the tested films. The wide range of results demonstrated the feasibility of using MCC as a polyol, indicating applications for the films generated as coatings, packaging, dressings, among others. As far as is known, the approach of this study is unprecedented.

D. S. Porto · A. Cassales · E. Frollini (✉)
Macromolecular Materials and Lignocellulosic Fibers Group, Center of Research on Science and Technology of BioResources, São Carlos Institute of Chemistry, University of São Paulo, CP 780, São Carlos, São Paulo 13560-970, Brazil
e-mail: elisabete@iqsc.usp.br

A. Cassales
Biomass Technology Laboratory, Embrapa Tropical Agroindustry, Fortaleza, Ceará, Brazil

H. Ciol · N. M. Inada
São Carlos Institute of Physics, University of São Paulo, São Carlos, Brazil

Graphical abstract
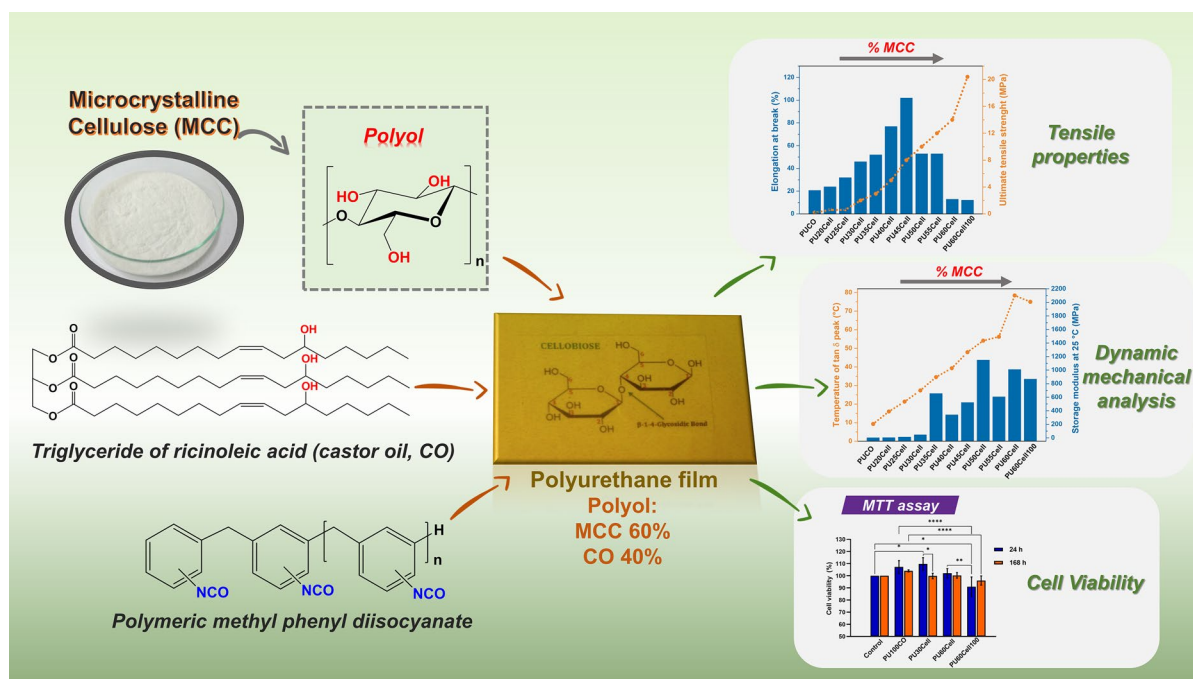
Introduction

PUs have a wide range of applications, such as the
production of fibers, resins, adhesives (Chen and Tai
2018), coating materials, foams, composites (Khan-
deray and Gite 2019), and electrodes (Wong et al.
2019), as well as being used for controlled release of
active ingredients (Liao et al. 2021), and films (Cas-
sales et al. 2020; Turan 2021). PUs are prepared from
the reaction between reagents containing at least two
isocyanate and hydroxyl groups, which results in the
formation of carbamate groups as the main character-
istic group in their chemical structure. In addition to
the use of isocyanates and polyols, different catalysts
(organic and organometallic) and solvents are com-
monly used in the synthesis of PUs (Reghunadhan
and Thomas 2017; Wang et al. 2019).

The synthesis of bio-based PUs, mainly under sol-
vent- and catalyst-free conditions, is of great interest.

This approach can lead to a lower environmental
impact, biodegradability, and other advantages when
compared to processes in which reagents from fos-
sil resources are used (Noreen et al. 2016; Lyu et al.
2019).

Polyols can be obtained from plant biomass with-
out chemical modification, such as the triglyceride of
ricinoleic acid present in castor oil (*Ricinus commu-
nis*) and lignin (Fig. 1) from lignocellulosic sources
or using chemical modifications, such as the transes-
terification and ozonolysis of fatty acids (Wang et al.
2019). In a previous study, Cassales et al. (2020)
synthesized bio-based PUs from polymeric diphe-
nylmethane diisocyanate (pMDI) and the main pol-
yol components of castor oil (namely the triglycer-
ide of ricinoleic acid) and kraft lignin (Fig. 1) under
catalyst- and solvent-free conditions. The previously
mixed reagents were spread on a flat surface, which
allowed the simultaneous formation of a film dur-
ing the synthesis. In another investigation, a widely
available lignin derivative, lignosulfonate, was used
as a polyol along with castor oil (CO). The synthe-
sis was also carried out under catalyst- and solvent-
free conditions in molds under different temperature

Fig. 1 Polyols obtained from oilseed (triglyceride of ricinoleic acid) and ligno-cellulosic biomass (lignin)
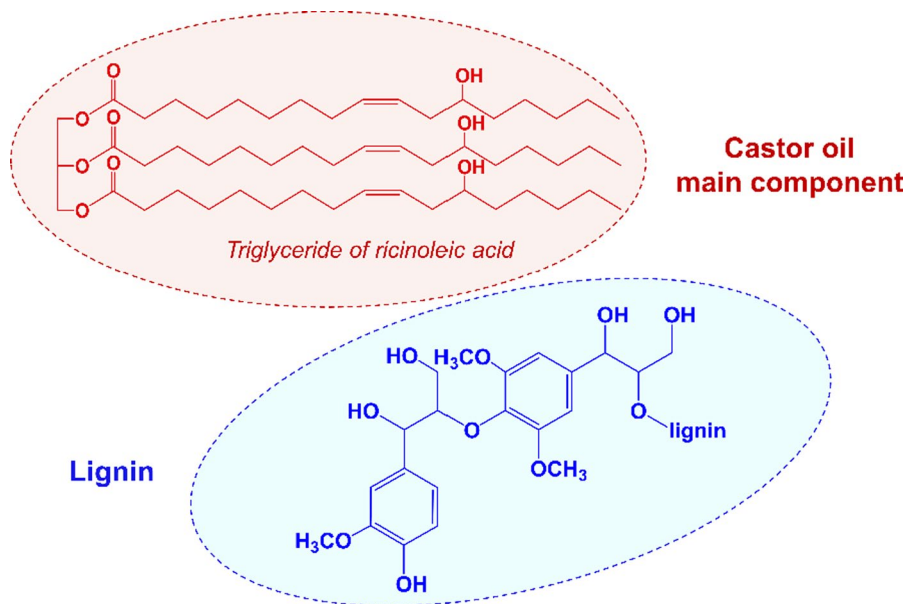
and pressure using lignocellulosic fibers mixed with the reagents, which enabled the simultaneous generation of bio-based composites during the synthesis (de Oliveira et al. 2020).

The vegetable oil platform is one of the most important for the production of new bio-based PUs because functionalized structures bearing OH groups can be obtained via chemical modification (e.g. epoxidation) or modification of their structure (e.g. transesterification/amidation). CO stands out because its use as a polyol does not require any chemical modification and it is widely available (Oliveira et al. 2015; Noreen et al. 2016; Gómez-Jiménez-Aberasturi and Ochoa-Gómez 2017; Lin et al. 2021). CO is mainly composed of the triglyceride of ricinoleic acid (~90%, Fig. 1), which has OH groups in its chemical structure (Belachew et al. 2021). In addition to acting as a polyol source, CO helps disperse the solid reagents used in the synthesis of bio-based PUs (Cassales et al. 2020; Oliveira et al. 2015).

The use of cellulose as a polyol is advantageous because it does not involve any prior steps.

As the most abundant plant polymer found on earth, cellulose is one of the main constituents of lignocellulosic biomass and has been widely explored due to its biodegradability, availability, and different characteristics, such as the mechanical properties of its fibers (Kontturi et al. 2021; Seddiqi et al. 2021) and diverse chemical derivatization (Sjahro

et al. 2021). Linear chains comprised of β-D-anhydroglucopyranose units with varying sizes linked via β-1,4 glycosidic bonds form the cellulose macromolecule and have hydroxyl groups linked to C_6, C_2, and C_3 (Fig. 2). These groups can act as nucleophiles or be modified via oxidation reactions (Zugenmaier 2008; Rodrigues et al. 2015; Seddiqi et al. 2021).

Despite the broad scientific knowledge involving chemical modification and biotechnological applications used to obtain polyols from carbohydrate platforms, the use of cellulose as a polyol in PU synthesis has been rarely reported in the literature.

The use of cellulose as a chain extender for the formation of PUs, which involves a low concentration of cellulose in the polymer formulation, has been reported in the literature (Solanki and Thakore 2015; Ikhwan et al. 2017). However, the use of microcrystalline cellulose (MCC)/cellulose as the primary polyol in the synthesis of PUs, as far as we know, has not been reported to date.

MCC, a partially depolymerized cellulose, is mainly obtained via the acid hydrolysis of bleached chemical pulps using hydrochloric acid (Hamad et al. 2019; Katakojwala and Mohan 2020). Recently, the use of MCC in materials has increased, for example, as a reinforcement material in composites (Ramires et al. 2020). The wide range of applications, together with its physical, biodegradability, and non-toxicity

Fig. 2 Chemical structure of cellulose and its use as a polyol
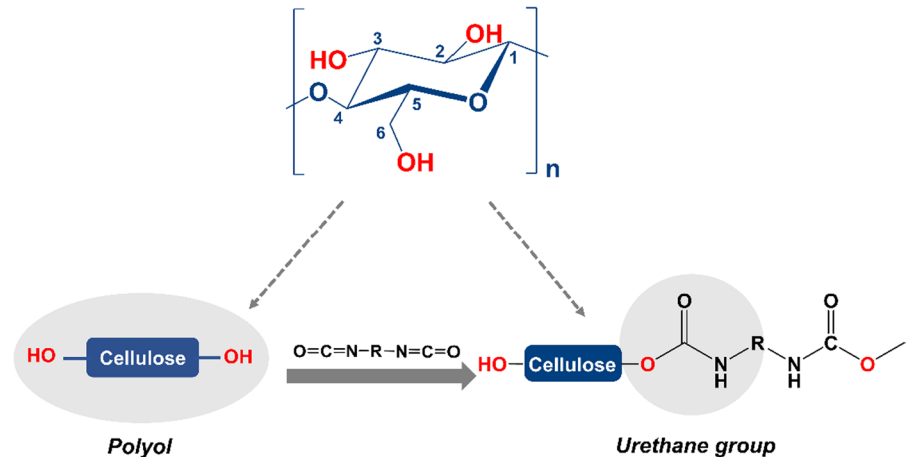
properties, has placed MCC in a prominent position (Katakojwala and Mohan 2020).

CO-based PUs (Su et al. 2019) and PU nanocomposites with bacterial cellulose membranes (Urbina et al. 2019) present moderate cell viability. CO-based PU composites prepared with MCC and cellulose nanocrystals as reinforcement materials show high cell viability (non-toxicity), indicating they are promising materials for biological applications (Villegas-Villalobos et al. 2018).

This study has investigated the synthesis of bio-based PUs prepared from low to the highest possible percentage of MCC as a polyol, CO, and pMDI in the absence of solvents and catalysts with simultaneous film formation at room temperature. The use of CO as a second polyol made the absence of solvent possible because it also acts as an MCC dispersing agent. The synthesis in which the highest proportion of MCC was used as a polyol was also carried out at 100 °C to compare the properties of the resulting film with those of the film generated at room temperature. Bio-based PU films have been evaluated for several properties, including biocompatibility, using their cell availability.

Briefly, the goal of this study was to investigate the bio-based synthesis of PUs using MCC as a polyol in the absence of a catalyst and solvent with the concurrent formation of films with properties suitable for a diverse range of applications.

Materials and methods

Materials

MCC was purchased from Valdequímica (São Paulo, SP, Brazil). CO (hydroxyl index = 155 mg KOH/g and average molar weight (Mn) = 980 g/mol, as provided by the supplier) was purchased from Azevedo Indústria e Comércio de Óleos Ltd. (Itupeva, SP, Brazil) and polymeric diphenylmethane diisocyanate (pMDI, Desmodur® 44V20L, 31.3% NCO groups, according to supplier information) was provided by Covestro (São Paulo, SP, Brazil). Copper (II) ethylenediamine was purchased from Qeel (São Paulo, SP, Brazil), N,N-dimethylformamide (DMF) was purchased from Sigma (São Paulo, SP, Brazil).

Methods

Synthesis of PUs

The synthesis of the PUs was carried out using molar values of MCC/CO between 20 and 60% with respect to the concentration of OH groups present in MCC and CO. The ratio of NCO/OH groups was 1:1 in all reactions based on the concentration of OH groups in CO (2.8×10^{-3} mol de OH/g) (Cassales et al. 2020) and MCC (18.5×10^{-3} mol de OH/g). The syntheses were carried out according to the following steps:

Step 1: 20 g of CO was placed in a 50 mL beaker and degassed for 30 min using a vacuum pump (Edwards,

RV-12, England). MCC was dried for 4 h at 105 °C in an air-circulating oven and added to the degassed CO (for the control film, PUCO, only CO was used as a polyol). The mixture was stirred using a mechanical stirrer at 110 rpm for 7 min and dispersed for 5 min using a sonicator (Sonics Vibra Cell, VC 505, USA, 20 kHz, 0.5 s cycles, 40% amplitude); this cycle was repeated twice.

Step 2: The MCC/CO dispersion and pMDI were degassed for 30 min. Then, in sequence, the mass of pMDI relative to the required NCO concentration was added to the CO/MCC dispersion, and the system was stirred for 5–10 min and taken to degas for 3–10 min (different times were used due to the distinct characteristics of each reaction mixture).

Step 3: From the visualization that the viscosity of the reaction medium was adequate for spreading it on a glass plate, this was done using a 1 mm extender, and the reactions proceeded on the plate surface, simultaneously with the formation of films. The reactions were carried out in an environment with controlled humidity ($30 \pm 5\%$) and temperature (25 ± 2 °C). For PU60Cell100, the reaction and film formation took place in an oven at 100 °C.

Regarding the polyols used in the formulation of PUs, CO was the component with the highest mass, as it has a lower content of hydroxyl groups than MCC. As the films were formed during the synthesis, 20 g of CO was adequate to generate films with the necessary dimensions to carry out all of the characterizations described hereafter (Sect. 2.1) and to disperse the MCC in the reaction medium. The percentage of MCC was calculated considering its average molar mass of 21,040 g/mol (Sect. 2.2.1) and hydroxyl index of $\sim 18.5 \times 10^{-3}$ mol of OH g^{-1} (389 mol of OH/21040 g of MCC), while for CO (molar mass = 977.2 g/mol) the hydroxyl index was 2.763×10^{-3} mol of OH/g of CO (2.7 mol of OH/977.2 g of CO).

Information on the MCC percentage and MCC/CO ratio (considering the concentration of OH groups) used in each synthesis is shown in Table 1.

The PU films formed during the syntheses were tested for solubility in various organic solvents, including tetrahydrofuran, acetone, 1-methyl-2-pyrrolidone, dimethylformamide (DMF), chloroform, ethyl acetate, dichloromethane, dimethyl sulfoxide

Table 1 Codes and information on the % of MCC, MCC/CO ratio with respect to the concentration of hydroxyl groups, and temperature (T) used in the synthesis of PUs-pMDI with simultaneous film formation

Film	MCC (%)	T (°C)	Ratio MCC/CO
PUCO*	–	25	–
PU20Cell	20	25	0.25
PU25Cell	25	25	0.33
PU30Cell	30	25	0.43
PU35Cell	35	25	0.54
PU40Cell	40	25	0.67
PU45Cell	45	25	0.82
PU50Cell	50	25	1.00
PU55Cell	55	25	1.22
PU60Cell	60	25	1.50
PU60Cell100**	60	100	1.50

PU polyurethane, *CO* castor oil, *Cell* cellulose

*100% CO as polyol, control film; **Glass plate placed in an oven with air circulation at 100 °C

(DMSO), and carbon tetrachloride. The concentrations were selected considering those typically used in size exclusion chromatography (SEC; average molar mass evaluation) and nuclear magnetic resonance (NMR; chemical structure evaluation) spectroscopy. There was no dissolution in any of the solvents and therefore, SEC and NMR analyses were not performed.

Characterization of reagents and films

Viscosity average molar mass

A glass capillary viscometer (Ubbelohde, f = 0.63 mm, AVS-350 Schott-Geräte, Germany) was used to evaluate the viscosity of MCC dissolved in an aqueous copper(II) ethylenediamine solution (TAPPI T230 om-08 standard; TAPPI 2008). MCC (0.030 g) was dissolved in copper(II) ethylenediamine solution (20 mL) under magnetic stirring for 30 min at 25 °C. The solution and solvent flow times were measured in triplicate. The intrinsic viscosity value, [η], was estimated from the flow times and converted into the DP value using Eq. 1 (Duan et al. 2015):

$$DP^{0.905} = 0.75[\eta] \qquad (1)$$

The viscosity average molar mass, MM$_{Vis}$, was estimated using Eq. 2:

$$MM_{Vis} = DP \times 162 \tag{2}$$

where 162 is the molecular weight of an anhydroglucose unit (g/mol).

Scanning electron microscopy

Scanning electron microscopy (SEM) analysis was performed using a 440 Zeiss DSM 940 instrument (Germany) at an acceleration voltage of 20 kV. Approximately 1 mg of MCC was used. For the analysis of the film surface, the samples were cut to a length and width of 1 cm. In the fractographic analysis, the samples were cut to a length of 3 cm and width of 0.5 cm, inserted in liquid nitrogen for 10 min, and then fractured using metal clamps. All samples were placed on carbon tape inserted in an aluminum sample holder and covered with a thin layer of gold (20 μm) using a Baltec Coating System metallizer (MED 020, Liechtenstein).

FTIR spectroscopy

The FTIR spectrum of MCC was acquired using an IRAffinity-1 Shimadzu instrument (Japan) in the wavenumber range of 4000 to 400 cm^{-1} at a resolution of 4 cm^{-1} over 32 scans using KBr pellets (1 mg of MCC and 100 mg of KBr). The FTIR spectra for CO and pMDI were obtained under the same conditions, however, the samples were deposited between silicon wafers.

FTIR spectra of the films were obtained using attenuated total reflectance (ATR) mode from 4000 to 650 cm^{-1} at a resolution of 4 cm^{-1} over 32 scans using samples with dimensions of 3 cm × 1 cm.

Thermogravimetric analysis

Thermogravimetric analysis (TGA) was performed using 8 mg of sample under an N$_2$ atmosphere at a flow rate of 20 mL min^{-1} and heating rate of 5 °C min^{-1} from 25 to 400 °C (MCC, CO, and pMDI), or from 25 to 900 °C (films) using a platinum support. A Shimadzu TGA-50 instrument (Japan) was used for the analysis.

X-ray diffraction

The MCC crystallinity index (CrI) was determined using X-ray diffraction (XRD) on a D8 Advance X-ray diffractometer (Bruker, USA) equipped with a LynxEye detector. The films were placed into capsules immersed in N$_2$, and then ground in a Mixer Mill Retsh MM 400 (Germany). The samples were oven-dried at 105 °C for 24 h, placed in a desiccator to stabilize the temperature for 20 min, and analyzed as a powder.

The PUCO, PU20Cell, PU30Cell, PU40Cell, PU50Cell, PU60Cell, and PU60Cell100 films were selected for X-ray diffraction analysis. The selection criterion was to consider the full extent of variation in the MCC content in the formulation of the PUs that generated the films. The analyses were performed at the Laboratory for the Synthesis and Characterization of Nanomaterials located at the Amazonas Federal Institute of Education, Science and Technology (Manaus, AM, Brazil) using a Bruker D2 Phaser diffractometer (Bruker AXS, Germany) with a slit width of 0.6 mm, knife of 3 mm, Cu radiation tube (K$_\alpha$ = 0.15406 nm, 30 kV, 10 mA),

Measurements were made in the Bragg angle (2θ) range of 5 to 60° with a step size of 0.02°and an irradiation time of 0.5 s per step.

The total area and the area under diffraction peaks were obtained from the diffractograms generated, and CrI was calculated using DIFFRAC EVA software, version 4.2 (Bruker, USA).

Polarized light microscopy

Polarized light microscopy (PLM) was performed on a CRAIC PV 20/30 microspectrometer (USA) equipped with a 40× objective lens and light angle variation of 0–90°; 1 cm × 1 cm samples were placed on glass slides. The PUCO, PU25Cell, PU30Cell, PU40Cell, PU45Cell, and PU55Cell films were selected from the results obtained, as will be described later.

Ultraviolet–visible spectroscopy

Ultraviolet–visible (UV–Vis) spectra were obtained on a Jasco V-630 spectrophotometer (Japan) from 300 to 800 nm with film dimensions of approximately 3 cm × 1.2 cm. To avoid interference from the material

thickness (0.67 ± 0.02 mm to 0.87 ± 0.01 mm), the absorbances were normalized using Eq. 3.

$$\text{Normalization} = \frac{absorbance}{thickness} \qquad (3)$$

The transmittance was obtained from the absorbance values normalized in Eq. 4, derived from the Lambert–Beer equation (Skoog et al. 2014).

$$\text{Transmittance} = 10^{\text{-normalized absorbance}} \times 100 \qquad (4)$$

The wavelength of 750 nm was selected to compare the change in the transmittance (%) between the formed films.

Contact angle

A CAM 200 KSV Instruments goniometer (Finland) equipped with a camera and recording system (São Carlos Institute of Physics, University of São Paulo) was used for contact angle measurements. A drop of deionized water (4 μL) was deposited on the surface of the PU film sample (1.0 ± 0.05 cm $\times$ 1.0 ± 0.05 cm) and the contact angle was evaluated in 300 s (1 frame/s), performed in triplicate, at 25 °C. The contact angles were calculated from a tangent adjusted to the contour of the drop at the point of contact between the film and the liquid using digital image analysis. The calculation was performed automatically using CAM 2008 image analysis software.

Swelling test

Swelling tests were performed according to the procedure described by Cassales et al. (2020). First, three samples of each film, with dimensions of 5 ± 0.2 mm $\times$ 5 ± 0.2 mm, were prepared. The samples were then pre-weighed and placed in vials containing 7 mL of DMF at room temperature. After 5 d, the films were dried on paper towels and re-weighed. The swelling (S%) was calculated using Eq. 5 (Jia et al. 2015).

$$S\% = \frac{M - M_0}{M_0} \times 100 \qquad (5)$$

where M is the swollen polymer mass (g) and M_0 is the dry polymer mass (g).

Dynamic mechanical analysis

Dynamic mechanical analysis (DMA) was performed using a DMA thermal analyzer (Q800, TA Instruments, USA) equipped with tension-mode film clamps. The samples were 5.2 mm $\times$ 6.3 mm $\times$ 0.70 mm in size (distance between clamps $\times$ width $\times$ thickness) and analyzed using the following parameters: oscillation amplitude of 20 μm, preload of 0.01 N, frequency of 1 Hz, heating rate of 3 °C min^{-1} (from -100 to 150 °C). At least three samples were tested for each film.

Tensile tests

Tensile tests were carried out at room temperature using a DMA Thermal Analyzer Q800 instrument (TA Instruments, USA) operated in tension film mode with a variation of 1 N min^{-1} up to 18 N, 0.001 N preload, and approximate dimensions of 5.2 mm $\times$ 1.15 mm $\times$ 0.7 mm (distance between clamps $\times$ width $\times$ thickness). At least three samples were tested for each film, which were stored in an environment with humidity of $30 \pm 5\%$ and controlled temperature of 25 ± 2 °C.

Biocompatibility evaluation

Cell viability

The cell viability of the PU films was evaluated by in vitro cytotoxicity, according to ISO 10993–5:2009 (International Organization for Standardization, ISO, 2009). The PUCO, PU30Cell, PU60Cell, and PU60Cell100 films were selected. The selection criterion was to consider the full extent of the variation in the MCC content in the film formulation. Samples measuring 1 ± 0.1 cm $\times$ 1 ± 0.1 cm were first sterilized in an autoclave for 20 min at 120 °C and then added to a plate containing 2.5 mL of Dulbecco's modified Eagle's medium (DMEM) supplemented with 5% fetal bovine serum (SFB) and kept under standard culture conditions (37 °C, 5% CO_2 and humidity) for 24 and 168 h.

Fibroblast cell suspensions of the HDFn line (Human Dermal Fibroblasts, neonatal—Gibco, catalog number C0045C) from Thermo Fisher Scientific (Waltham, MA, USA), cultivated in DMEM culture medium supplemented with 10% FBS, were

transferred to plates with a density of 2×10^4 cells per well upon reaching 80% confluence and maintained under standard culture conditions. After 24 h, the cells were washed twice with PBS (Phosphate Buffer Saline), and the extract in which the films (removed) were inserted (100 μL per well) was added to the cell wells, and maintained for 24 h. The medium was removed and the wells were washed twice with PBS before incubation with a 1 mg mL^{-1} solution of MTT (3-(4,5-dimethylthiazol-2-yl)-2,5-diphenyltetrazoli-umbromide) for 4 h at 37 °C. The resulting formazan crystals (violet coloration) solubilized in DMSO and the resulting colored solution was measured by UV–Vis spectrophotometry. The cell viability was determined indirectly without contact between the films and cells upon comparison with the control group, which remained incubated with DMEM medium supplemented with 5% FBS, and expressed as a percentage of viable cells according to Eq. 6:

$$Cell\,viability(\%) = \frac{Absorbance\,of\,samples\,and\,fibroblasts}{Absorbance\,of\,control} \times 100$$

(6)

The results represent the mean ± standard deviation (SD) of the data normalized for the controls from five experiments. Statistical analysis was performed using two-way ANOVA with Tukey's comparison.

Results and discussion

Characterization of MCC, CO, and pMDI

The MM$_{vis}$ of MCC obtained from viscometry analysis was $21,040 \pm 72$ g/mol, which is similar to that reported in a previous study (Kaschuk and Frollini 2018). The hydroxyl index for MCC (18.5×10^{-3} mol de OH/g) showed a high concentration of OH when compared to other macromolecules, such as lignin (Tolbert et al. 2014; Cassales et al. 2020), as expected, because each repetitive unit of cellulose has three hydroxyl groups (Fig. 2).

The micrographs show that the fibrous structure of the starting material remains in the MCC after acid hydrolysis, which can be generated on a commercial scale. The fibers have a cylindrical shape, which can be better visualized in the magnified image in the insert of Fig. 1SI (Supplementary Information).

The X-ray diffractogram in Fig. 2SI show the presence of the characteristic peaks of cellulose. The most intense peak was observed at $2\theta = 22.6°$ and the other lower intensity peaks correspond to the typical reflection planes of cellulose I (Lin et al. 2013; French 2014; Ahvenainen et al. 2016). MCC exhibited a CrI of 56%, which is similar to that observed in the literature for MCC (56.3%) (Zheng et al. 2018).

The FTIR spectrum obtained for MCC (Fig. 2SI) exhibits a band at 3341 cm^{-1}, which was related to the stretching or axial deformation of the O–H bonds with contributions from intra- and intermolecular hydrogen bonds. The band observed at 2897 cm^{-1} was characteristic of the stretching of the C-H bonds and the intense band at 1056 cm^{-1} refers to the axial deformation of the C–OH bonds in the glucose rings. The peak observed at 1190 cm^{-1} corresponds to the deformation of the C–O–C bonds and the peak at 1383 cm^{-1} can be attributed to the CH$_2$ bond vibrations (Ramires et al. 2020).

The characteristic bands of the CO components were observed in the FTIR spectrum (Fig. 3aSI). The band at 3422 cm^{-1} was related to the O–H bond and an asymmetric stretching vibration at 2929 cm^{-1} and symmetric stretching at 2858 cm^{-1} corresponding to the C-H bonds of the CH$_2$ groups in the chemical structure of CO. The band observed at 1741 cm^{-1} was attributed to the deformation of the C=O bonds and the peak at 1167 cm^{-1} corresponds to the C-O bonds, which are present in the main components of CO, the triglyceride of ricinoleic acid (Fig. 1).

Figure 3bSI shows the FTIR spectrum obtained for pMDI, in which the high-intensity band observed at 2275 cm^{-1} was related to the isocyanate groups (-N=C=O). The band at 1522 cm^{-1} was attributed to the double bond deformation (C=C) of the aromatic rings present in pMDI. Other bands such as those observed at 816 and 3034 cm^{-1} were correlated to the deformation and stretching of the C-H bonds in the aromatic ring of pMDI, respectively (Wong and Badri 2012).

The dTG curve obtained for MCC (Fig. 3cSI) exhibits a peak at 53 °C, which can be attributed to the loss of adsorbed water due to the interaction of water with the polar regions of cellulose via the OH groups. Up to a temperature of 250 °C, it can be considered that MCC presents thermal stability because there was no thermal decomposition observed. The maximum mass loss velocity occurred at ~342 °C

(dTG peak temperature) with decomposition in the range of 279–400 °C. Thermolysis reactions occur in cellulose (> 300 °C) via cleavage of the glycosidic bonds, C–C, C-H, and C-O bonds, dehydration, and decarbonylation. These reactions lead to the breakage of bonds in different regions of the cellulose chains (Scheirs et al. 2001; Ramires et al. 2020).

For CO, the temperature at which the maximum mass loss velocity was observed was 404 °C (Fig. 3dSI), which corresponds to the decomposition of the chain in the triglyceride of ricinoleic acid and was consistent with the literature (~ 388 °C) (de Oliveira et al. 2020).

The dTG curve obtained for pMDI (Fig. 3eSI) shows three regions of mass loss. The first peak at 298 °C was attributed to the initial formation of the carbodiimide group.

(-N=C=N-), which led to the release of CO_2. The second peak at 346 °C can be related to the oxidation or polymerization of carbodiimide, leading to the formation of polycarbodiimide and the release of CO_2. The third peak at 477 °C was related to the decomposition of the polycarbodiimide and carbodiimide groups, which was consistent with that described in the literature (~ 500 °C) (Zhang et al. 2014; da Silva et al. 2018).

Characterization of the PU films

The synthesis of PUs from MCC, CO, and pMDI can lead to structures similar to the shown in Fig. 4SI. The nuclear magnetic resonance spectra of the synthesized PUs are not available due to their insolubility, as mentioned, and the structure shown is suggested as a possibility only to illustrate the type of structure that could be generated. Although cellulose has a linear chain similar to pMDI (oligomer), the reaction between them, which also involves the triglyceride of ricinoleic acid present in CO, may generate a branched chemical structure, which may lead to cross-linking.

PUs are formed from MCC, CO, and pMDI via nucleophilic attack of the oxygen atom (OH group present in MCC and the triglyceride of ricinoleic acid in CO) to the electrophilic carbon atom present in the –N=C=O isocyanate group. The subsequent transfer of protons from the OH group to the N atom leads to the formation of a carbamate/urethane group (–OCONH–), Fig. 4SI.

FTIR spectroscopy

Figure 3 shows the FTIR spectra obtained for PUCO, PU30Cell, and PU60Cell. The band observed at 3339 cm⁻¹ was related to the N–H bonds of the carbamate groups formed, which does not have "shoulders" and suggests the non-incorporation of the -OH groups, which, if present, will be in insufficient concentrations to generate such "shoulders". This indicates that practically all of the OH groups originating from CO and MCC react to form urethane groups. The band observed at 3010 cm⁻¹ was related to the stretching of the C=C bonds with deformations at 1596 cm⁻¹, which were attributed to the aromatic rings present in pMDI and the unsaturated bonds in the aliphatic chain of the triglyceride of ricinoleic acid. The band at 2924 cm⁻¹ was related to the C–H bonds of the sp^3 carbons present in the MCC skeleton inserted in the chemical structure of PU and the band at 2854 cm⁻¹ was related to the C–H bonds of the saturated hydrocarbons present in the triglyceride of ricinoleic acid (Wong and Badri 2012; Ramires et al. 2020).

The absence of a band at 2275 cm⁻¹ was observed in all of the films, indicating that the NCO groups fully reacted to form urethane groups (Ramires et al. 2020). The bands corresponding to the urethane groups were observed at 1726 (C=O bond stretching), 1310 (axial deformation of C–N bonds), and 1523 cm⁻¹ (out-of-plane deformation of N–H bonds). The intense bands observed at 1216 and 1044 cm⁻¹ correspond to the CO ester bonds involving the –OH groups of CO and MCC
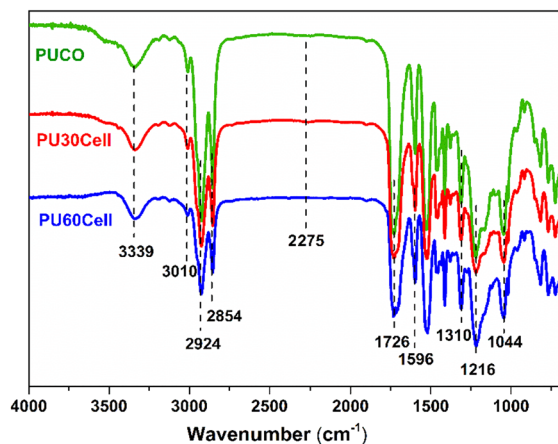

Fig. 3 FTIR spectra obtained for the PUCO, PU30Cell and PU60Cell films

that react to form carbamate bonds with pMDI (Wong and Badri 2012; Mathew et al. 2018). The spectra obtained for the other films (not shown) were similar to those of the PU30Cell and PU60Cell films (Fig. 3).

Scanning electron microscopy

Figure 5SI shows the surface of the PU50Cell and PU60Cell100 films; the other PUs-pMDI films exhibited micrographs (not shown) with surfaces similar to the shown in Fig. 5SI. The surface micrographs of the films formed during the PU synthesis show uniformity and no imperfections.

The micrographs of the fractured surfaces of the PUCO, PU25Cell, PU30Cell, PU35Cell100, PU40Cell, PU45Cell, and PU55Cell films show similar morphological features (Fig. 4). Structures that suggested spherulites were observed, which led to the analysis of such regions using polarized light microscopy.

The fracture surface micrographs of the PUCO, PU25Cell, PU30Cell, PU35Cell100, PU40Cell, PU45Cell, and PU55Cell films show circular regions in distinct parts of the analyzed portions. Parts of these regions may correspond to spherulites (see polarized light microscopy images in the insets of Fig. 4), whose structures were possibly formed during polymer crystallization (Crist and Schultz 2016). In the present study, they may have been formed during the synthesis of the PUs and film formation steps.

Spherulite formation has already been observed during fusion crystallization in PUs composed of hard segments (HS) generated using MDI as a reagent, which leads to crystalline domains and soft segments (SS), such as poly(tetramethylene ether) glycol (PTMG) and normally constitute the non-crystalline region. The spherulites had a diameter of ~30 μm (Yanagihara et al. 2017).

Crystalline domains can organize themselves to generate fibrils, which can grow radially from the center, usually with irregular branches, forming spherulites. The spaces between the bundle-like structures usually correspond to the non-crystalline domains (Crist and Schultz 2016). When bundle-like structures are observed, it is possible to find the HS domains stacked inside them, such that the SS regions are oriented perpendicular to the HS domains (Yanagihara et al. 2017).

From the polarized light microscopy images shown in Fig. 4, it is possible to observe a 90° light deviation at the edges of spherical formations (highlighted in the images) and bundle-like structures, which suggests that spherulite-type structures were created during the synthesis of the PUs with simultaneous film formation.

The fracture surface micrographs of the PU20Cell, PU35Cell, PU50Cell, PU60Cell, and PU60Cell100 films show similar morphological features, which are grouped in Fig. 5.

The micrographs of the cryofractured PU20Cell and PU35Cell films show circular regions (Fig. 5), which do not show any polarized light deviations (which is characteristic of spherulites), but indicate the points at which the fracture of the films started (Battjes 2004). Fiber-like morphologies were observed in a few regions, which can be attributed to the unreacted MCC (Fig. 1S1). It is noteworthy that fibers were not visually observed, nor bands corresponding to hydroxyl groups observed in the FTIR spectra of the films (Fig. 3), indicating that the MCC mainly reacted to form the PUs that generated the films. PU60Cell showed cavities, probably due to the displacement of the MCC fibers.

Fracture surfaces with uneven relief were observed when high concentrations of MCC were used as a polyol (e.g., PU60Cell), unlike that observed for films such as PU20Cell (Fig. 5). This suggests that the film formed using the higher % of MCC suffered ductile deformation (Yuwawech et al. 2017) because of the increased rigidity of the chemical structure of the synthesized PU that generated it. The PU60Cell100 film presents wavy and grooved fracture surfaces, indicating that the synthesis at 100 °C led to a film with a different internal morphology to the others films formed at 25 °C.

X ray diffraction

The X-ray diffractograms obtained for the selected films (Fig. 6SI) show intense 2θ peaks at ~19.5°, ranging between 19.1° (PUCO) and 19.8° (PU60Cell), as well as low intensity peaks at ~7.3°, attributed to the regular interplanar spacing of the rigid segments (Trovati et al. 2010; Ghobashy and Abdeen 2016).

The diffractograms (Fig. 6SI) showed CrI values > 70%, even for the control film (76%, Table 2),

Fig. 4 Fracture surface micrographs of **a** PUCO, **b** PU25Cell, **c** PU30Cell, **d** PU40Cell, **e** PU45Cell and **f** PU55Cell; the insets (on the right) show the polarized light microscopy images of selected regions that suggest the formation of spherulites should be at "Scanning Electron Microscopy."
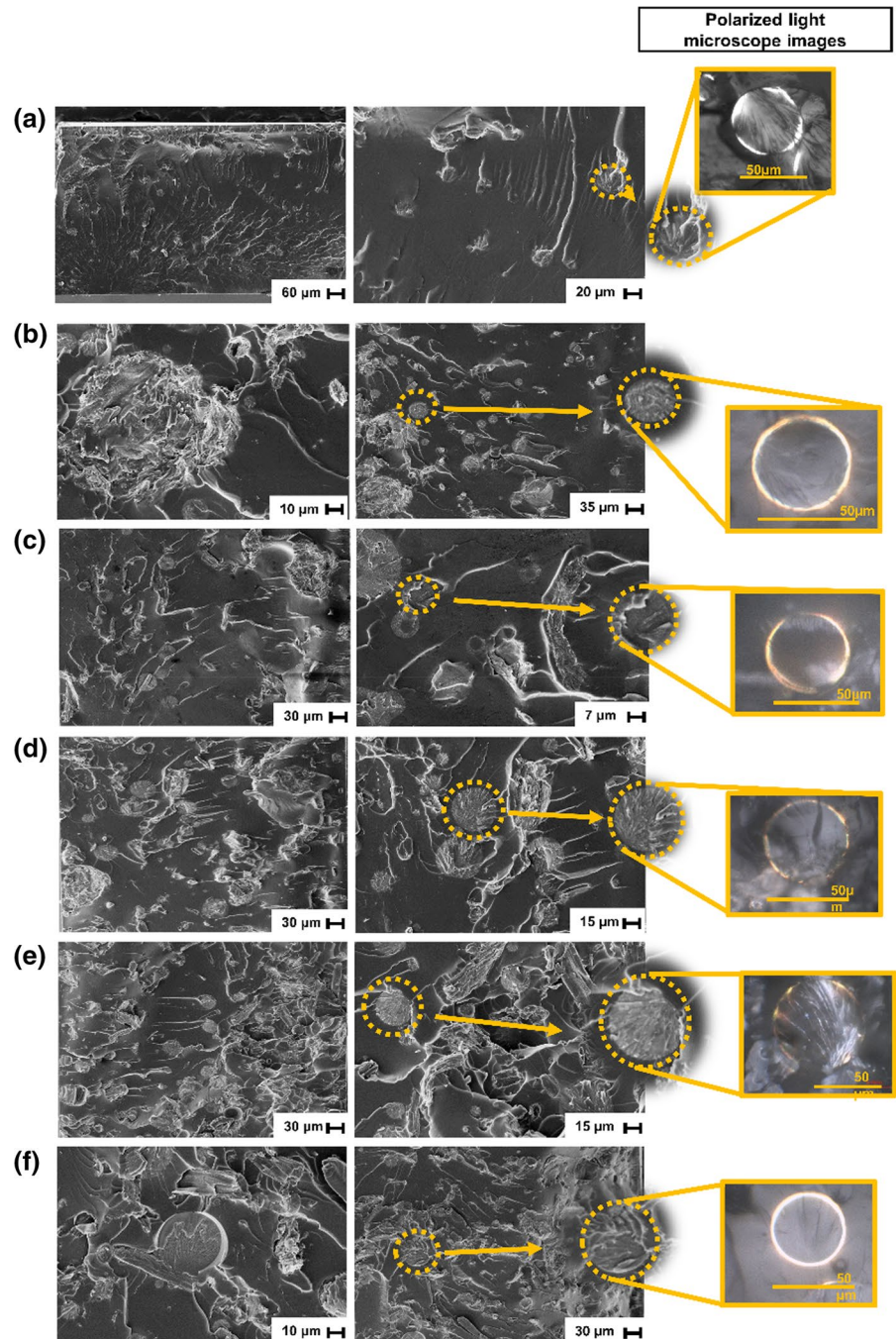

indicating that the rigid segments originating from pMDI (Fig. 4SI) are mainly responsible for the crystalline regions, even if they are present in structures with different complexities, when compared to the chemical structure generated upon the reaction

between CO and pMDI, and those generated when part of the CO was replaced by MCC.

The values observed for the CrI of the PUs in Table 2 (74–76%) show that the crystallinity, considering the built-in errors of the analysis (not measured due to issues of accessibility to the equipment in the period

Fig. 5 Fracture surface micrographs of the **a** PU20Cell, **b** PU35Cell, **c** PU50Cell, **d** PU60Cell, and **e** PU60Cell100 films
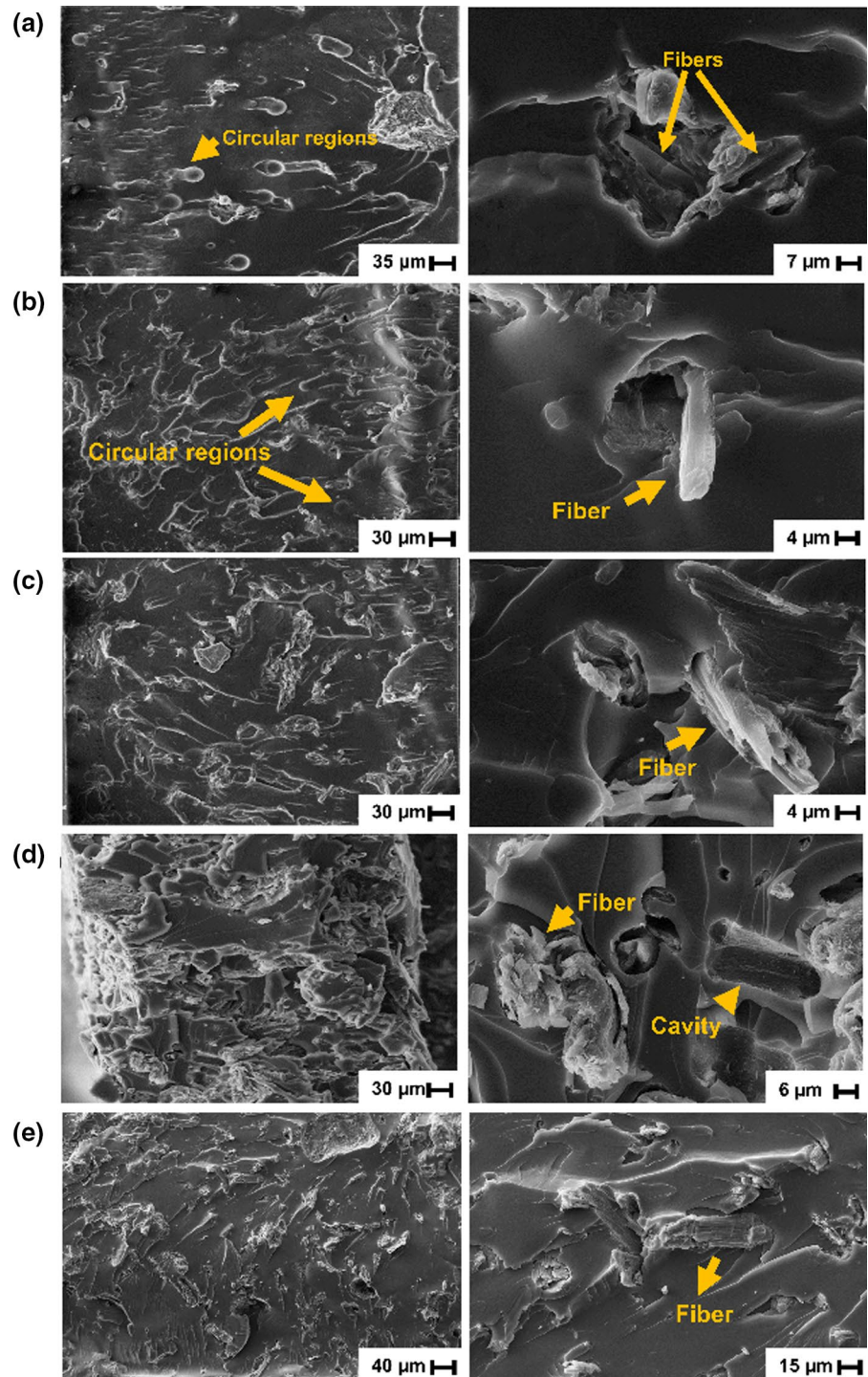
of analysis), did not change when part of the CO was replaced by MCC as the polyol. When MCC was used as a polyol, there was a greater amount of structures originating from pMDI due to the high concentration of –OH groups in MCC, which requires a larger amount of –NCO groups to react. Even with the increase of typical pMDI structures, the crystallinity was not altered, being similar to that of PUCO (control).

Table 2 Crystallinity index (CrI) of the PUCO, PU20Cell, PU30Cell, PU40Cell, PU50Cell, PU60Cell, and PU60Cell100 films

Film	CrI (%)
PUCO	76
PU20Cell	76
PU30Cell	75
PU40Cell	76
PU50Cell	74
PU60Cell	75
PU60Cell100	74

The CrI values obtained for the PUs/MCC, Table 2, were close to those observed for PUs synthesized from CO, polyethylene glycol-1000, and toluene diisocyanate (TDI) (~70%) (Morsi and Mohamed 2017), as well as for PUs prepared from castor oil, TDI, and cellulose-acetylated nanocrystals (used as reinforcement) (74%) (Lin et al. 2013). PU60Cell100 did not show any variation in the CrI when compared to PU60Cell,

indicating that the creation of the crystalline regions was unresponsive to the variation in the synthesis temperature from 25 to 100 °C.

It is noteworthy that the diffractograms of the PUs/MCC exhibit profiles and peaks with intensities similar to those found for PUCO without the presence of MCC in its formulation. This indicates that the small percentage of unreacted MCC fibers observed in the micrographs of some of the films (Fig. 4) did not change the crystalline region of the PUs, indicating the presence of a very small amount of fibers in the obtained films.

Optical properties

The PU/MCC films are transparent when different concentrations of MCC were used as a polyol, as shown in Fig. 6. A yellow color was observed, which possibly arose from the typical structures of pMDI (which exhibits a brown color). For PU60Cell100, a more intense yellow–brown color was observed.
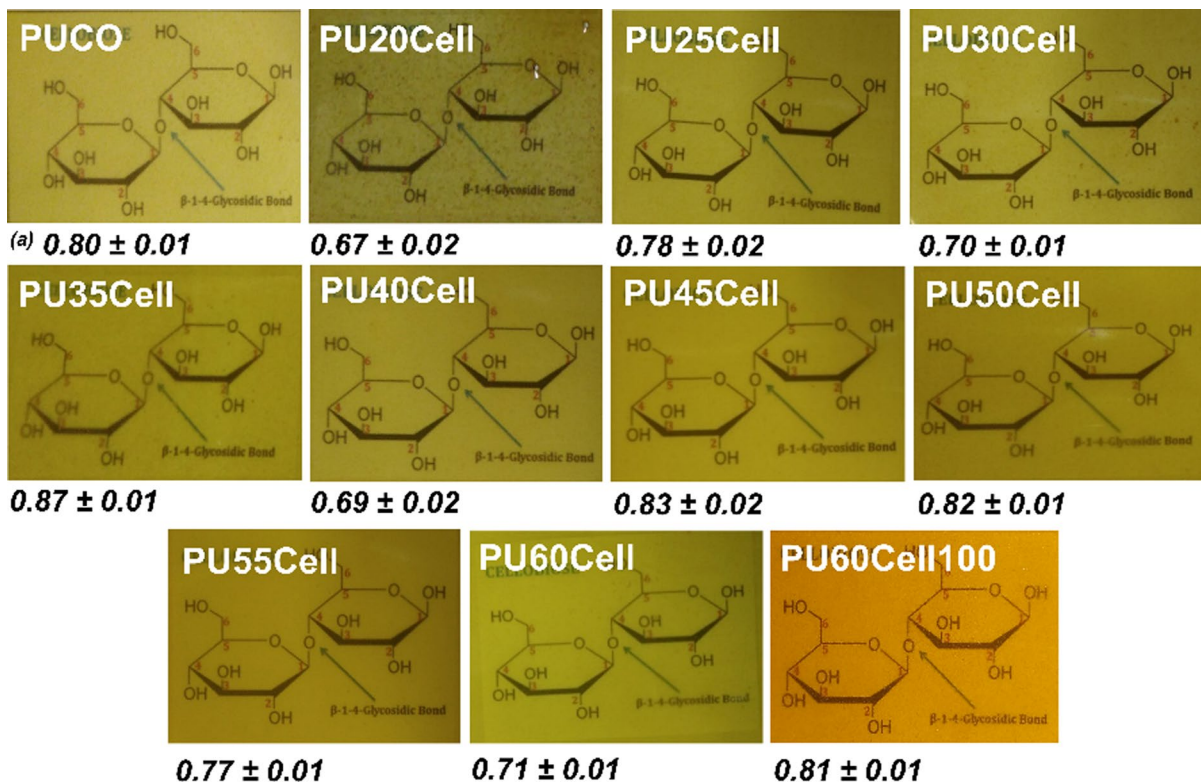

Fig. 6 Photographs and thicknesses for the films formed during the synthesis of the PUs. **a** Average film thickness (mm)

Table 3 Transmittance observed at 750 nm for the films formed during the synthesis of the PUs

Film	Transmittance (%)
PUCO	10.8
PU20Cell	5.7
PU25Cell	4.4
PU30Cell	6.3
PU35Cell	4.3
PU40Cell	2.7
PU45Cell	2.7
PU50Cell	2.7
PU55Cell	2.2
PU60Cell	2.0
PU60Cell100	3.9

The UV–Vis spectra of the PU films are shown in Fig. 7SI and the transmittance observed at 750 nm of the respective films are shown in Table 3.

The transmittance refers to the percentage of light transmitted by a material or medium and the degree of transparency is directly proportional to the transmittance. Polymeric films with transparency and good thermal and mechanical stability have attracted attention for various applications, such as packaging and the production of solar cells (Ni et al. 2015; Yuwawech et al. 2017). Aromatic groups (such as those present in pMDI) typically reduce the transparency due to their light absorption (Ni et al. 2015; Lan et al. 2019). All of the films exhibited transparency, however, those formed during the syntheses in which MCC was one of the polyols presented a lower transmittance than the control (PUCO) (Fig. 7SI). As mentioned, the higher the concentration of MCC in the PU formulation, the higher the amount of pMDI required for the synthesis due to the high concentration of OH groups in cellulose. Thus, the decrease in the light transmission of the films can be attributed to the high concentration of aromatic rings arising from pMDI.

It is noteworthy that the higher concentration of MCC in the PU formulation requires a higher amount of pMDI during the synthesis because of the high concentration of OH groups in cellulose, as mentioned beforehand. Thus, a decrease in the light transmission was expected for the films prepared using high concentrations of rigid aromatic structures

originating from pMDI, which promote the reduction in the transmittance (Lan et al. 2019).

The PU60Cell100 film (formed at 100 °C) shows a higher transmittance than the corresponding films generated at room temperature. The greater extent of the reaction at high temperature compared to the other PU films, as well as the possible formation of allophanate and biuret groups from secondary reactions capable of occurring at temperatures > 90 °C (Güney and Hasirci 2014), may have altered the polymeric structure and optical properties of the film, favoring an increase in the transparency of the material.

It is important to highlight that the films did not show any significant variation in their crystallinity (Fig. 6SI) and the presence of crystalline domains did not affect their transparency.

Thermographic analysis

Figure 7 shows the TG and dTG curves obtained for PU50Cell; the other films exhibit curves (not shown) similar to those shown and the results described in Table 4.

Three stages of mass loss were observed in the dTG curve obtained for PU50Cell (Fig. 7). The first event in the region between 240 and 360 °C (T_p = the temperature at which the rate of weight change was at its maximum, 343 °C) was related to the breaking of urethane bonds and decomposition of the MCC structures introduced into the macromolecule structure. This results in a weight loss of 17%. The second, between 360 and 440 °C (T_p = 386 °C), was related to
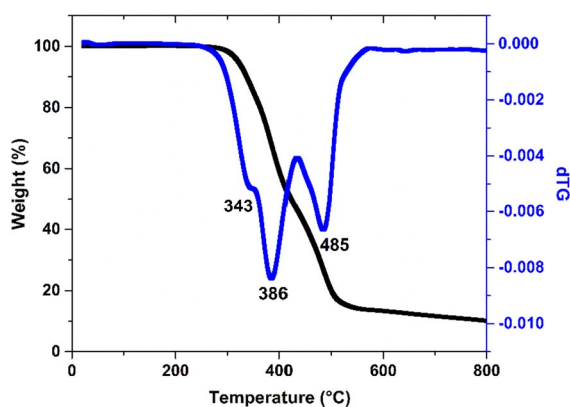

Fig. 7 TG and dTG curves obtained for PU50Cell (N_2 atmosphere, flow rate = 20 mL min^{-1}, heating rate = 5 °C min^{-1}) should be at "Thermogravimetric analysis"

Table 4 Temperature of the thermal events, % weight loss in the events, and residue of the PU films formed in the syntheses performed at room temperature

Film	T_{onset} (°C)	Event 1		Event 2		Event 3		Residue at 900 °C (%)
		T_p (°C)	Weight loss (%)	T_p (°C)	Weight loss (%)	T_p (°C)	Weight loss (%)	
PUCO	201	339	12	397	46	484	31	6
PU20Cell	237	345	14	391	45	478	29	7
PU25Cell	237	344	14	388	44	478	28	8
PU30Cell	242	345	16	391	40	482	30	7
PU35Cell	240	343	17	387	35	482	35	7
PU40Cell	245	344	15	388	39	477	34	8
PU45Cell	243	345	17	388	25	482	42	9
PU50Cell	248	343	17	388	36	483	32	9
PU55Cell	243	348	17	386	34	488	34	11
PU60Cell	243	345	19	386	31	483	35	11
PU60Cell100	248	348	20	388	34	482	31	9

the decomposition of the flexible segments of the PU chain, which in this case corresponds to the chains introduced from CO, with a weight loss of 36%. The third stage, in the region between 440 and 570 °C ($T_p = 485$ °C), can be attributed to the decomposition of the aromatic rings present in the isocyanate used (pMDI) (de Oliveira et al. 2020). The weight loss for this stage was 32% and a 9% residue was observed, which was related to coal formation, a result close to that observed for the other films (Table 4).

Table 4 shows that, in general, the films formed in the syntheses in which MCC was used in a greater proportion show an increase in the percentage of weight loss during event 1 and a decrease in event 2. The highest percentage of polyol MCC consequently promotes the greater presence of typical cellulose chains (event 1) and the reduced concentration of ricinoleic acid triglyceride (event 2). The initial decomposition temperature (T_{onset}) was shifted to a higher value upon increasing the concentration of MCC.

For the PU60Cell100 film, no significant changes were observed in the weight variations and during the different events when compared to the PU60Cell control film obtained at room temperature.

Contact angle

Figure 8 shows the results of the contact angles of the films studied. A contact angle of < 90° indicates a hydrophilic surface and the degree of hydrophilicity

increases as the angle decreases to 0°, which is considered to be a superhydrophilic material. Angles between 90 and 180° indicate a hydrophobic surface. Materials with angles close to 90° have an intermediate degree of hydrophilicity/hydrophobicity (Dwivedi et al. 2017).

The initial advance angles (t = 1 s) and equilibrium (t = 300 s) are shown in Fig. 8, together with photographs of the drops after 1 s of contact with the surface of the materials.

The films evaluated using contact angle measurements show a regular surface (Fig. 8, as observed in the micrographs in Fig. 5SI), which allows the analysis of the contact angle without significant interference from the surface morphology at the external angles of the drops.

The contact angles of the films formed during the PU synthesis at room temperature (25 °C) show similar results and a variation in the initial angles (t = 1 s) between 86 and 92° (Fig. 8), indicating films with intermediate grades of hydrophilic/hydrophobic character (Dwivedi et al. 2017) due to the presence of the segments introduced by CO and pMDI (hydrophobic) and hydrophilic groups, such as H-NCOO- in the urethane groups. Considering the errors embedded in the mean values of the informed angles, there was no significant variation when MCC was used as a polyol, which was a consequence of practically all of the hydroxyl groups in the macromolecule being reacted during the synthesis of the films. The slight variations observed, such as in PU60Cell100, can be

Fig. 8 Initial advancing angles and equilibrium angles observed for the films formed during the PU synthesis. *Error: Initial angle = [range from ± 1.1 (PU55Cell) to ± 6 (PU25Cell)]; Equilibrium angle = [range from ± 0.1 (PU55Cell) to ± 6.2 (PU25Cell)]
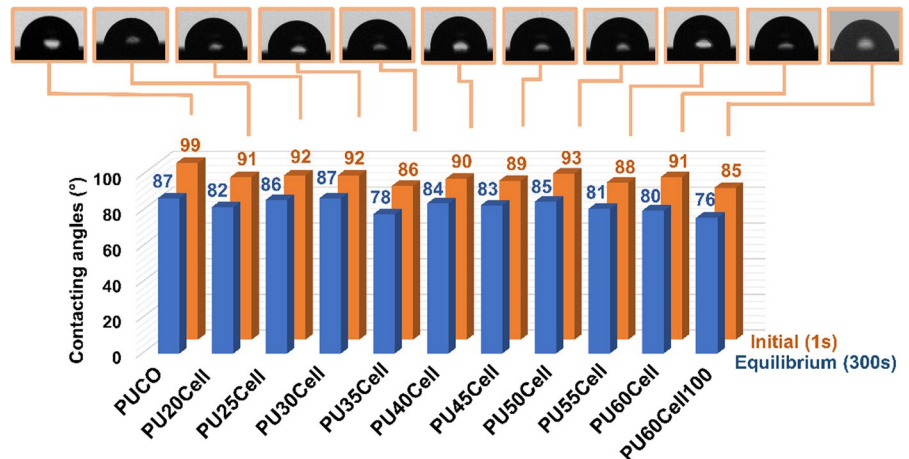
attributed to a greater number of isocyanate groups oriented towards the surface of the material. A similar behavior was observed for the equilibrium advancing angles (t = 300 s).

The homogeneous and smooth surfaces observed in the micrographs of the films (Fig. 5SI) led to a non-significant variation between the initial and equilibrium angles (of up to 11°), which also indicates the chemically homogeneous surface of the PU films obtained.

Swelling test

The degree of swelling can be considered as an indication of the available intermolecular volume (Cao et al. 2017; Cassales et al. 2020). In this study, the aim was to evaluate the interaction between an organic solvent (DMF) and the films formed during the PU synthesis. The films were immersed in DMF, the results shown in Fig. 9.

A highest swelling rate was observed for PUCO (control), Fig. 9, indicating the greater free volume available to accommodate DMF when compared to the other films. This is because the chemical structures of the macromolecules that make up the PUCO film have a greater number of flexible segments when compared to the other films in which MCC was also used as a polyol. The complexity of the chemical structures increases when MCC was used as a polyol, decreasing the free volume and capacity of the films to absorb DMF. From PU40Cell to PU60Cell, the absorption capabilities did not change significantly.
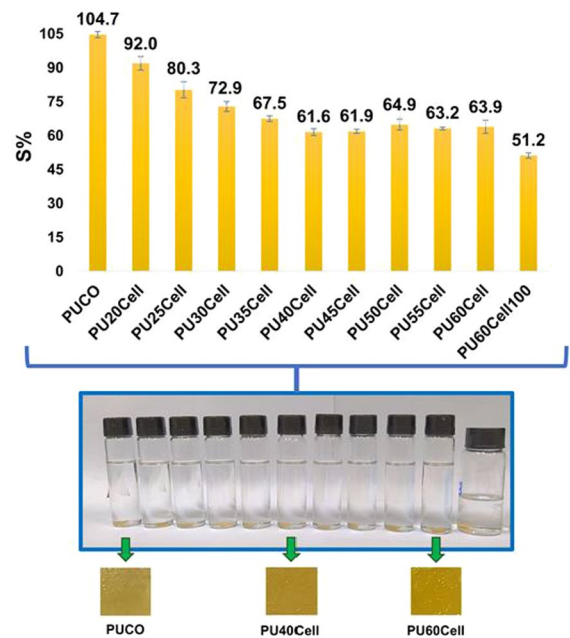

Fig. 9 Swelling tests for the PU films and photographs of the films in DMF after the end of the test. The vials contained in the photograph represent the films in the same sequence shown in the graph; the three photographs below the vials show the films after the test is over and represent all of the formed films

PU60Cell100 exhibited lower swelling (51.2 ± 1.2%) than PU60Cell (63.9 ± 2.9%), Fig. 9, indicating that when the reaction temperature was increased to 100 °C, the generated structures lead to a lower amount of free volume available. This may be due to secondary reactions that occur at 100 °C, which may result in the generation of allophanate

and biuret-type bonds (Sawpan 2018), leading to a decrease in the free volume available to accommodate DMF.

The photographs shown in Fig. 9 reveal that even after seven days, there was no partial dissolution of the PU films in DMF, as indicated by the transparency of the liquid medium, and also because the films remained entire; the tiny bubbles observed on the surfaces are due to the swelling of the films (photographs below the vials).

Dynamic-mechanical analysis

The temperatures of the tan δ peak and storage modulus at 25 °C for the PU films are shown in Fig. 10.

The tan δ curve was obtained using the ratio between the loss modulus (E') and storage modulus (E') (tan δ = E″/E'). The tan δ peak temperature can be related to the glass transition temperature (T_g), which is associated with single bond rotations involving the sp^3 carbons and heteroatoms, when present, in the segments of the macromolecules in the non-crystalline domain. The PU/MCC films show similar CrI values (~75%, Table 2), indicating that the non-crystalline domains account for ~25% of the total.

The film formed in the synthesis in which only CO was used as a polyol (PUCO) showed a T_g at 9 °C (Fig. 10), which was lower than that found for the films in which MCC was used as a polyol in addition to CO, reflecting the influence of the cellulose
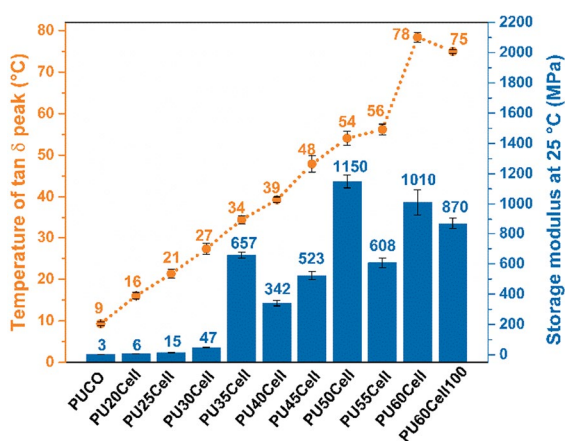

Fig. 10 Temperatures of tan δ peak and storage modulus at 25 °C for the PUCO, PU20Cell, PU25Cell, PU30Cell, PU35Cell, PU40Cell, PU45Cell, PU50Cell, PU55Cell, PU60Cell, and PU60Cell100 films

skeleton on the chemical structure of the PUs with respect to the glass transition temperature.

The films generated from the syntheses in which a higher proportion of MCC was used in the formulation have a lower proportion of flexible structures typical of the contribution from CO, promoting an increase in the rigidity of the macromolecular structure. Thus, rotations involving the single bonds present in the segments of the macromolecules, which characterize the T_g, will require a larger amount of thermal energy, and occur at higher temperature (Fig. 10). This promotes a variation in the T_g values between temperatures below, near, and above room temperature. The film formed simultaneously during the reaction performed at 100 °C (PU60Cell100) did not show any significant variation in T_g when compared to PU60Cell, which was formed at 25 °C. The possible formation of allophanate and biuret groups at 100 °C, as indicated by the swelling test, did not affect the glass transition temperature of the material.

For the PUCO, PU20Cell, PU25Cell, and PU30Cell films, the storage modules were quantified at 25 °C, a temperature above those found for the Tg of the respective films (Fig. 10). Thus, at 25 °C, the materials were under the action of the movement of the segments of chains present in the non-crystalline regions. This led to the lower storage modulus at 25 °C observed for the films with Tg values below room temperature. The storage modulus values at 25 °C observed for the films formed during the syntheses with formulations containing ≥ 35% MCC ($T_g > 25$ °C) were higher than those formed in the syntheses where the proportion of MCC was ≤ 35% ($T_g < 25$ °C), but do not correlate with the variation in the proportion of MCC used in the formulation of the PUs that generated the films.

Tensile properties

The tensile strength, elongation at break, and Young's modulus are shown in Fig. 11.

Figure 11 shows that increasing the percentage of MCC in the PUs increases the tensile strength of their respective films. The presence of a larger amount of typical MCC structures increases the proportion of rigid segments and the structural complexity of the PUs, which leads to materials that require a more intense force to rupture their resulting films (Marcovich et al. 2006; Rodrigues et al. 2015).
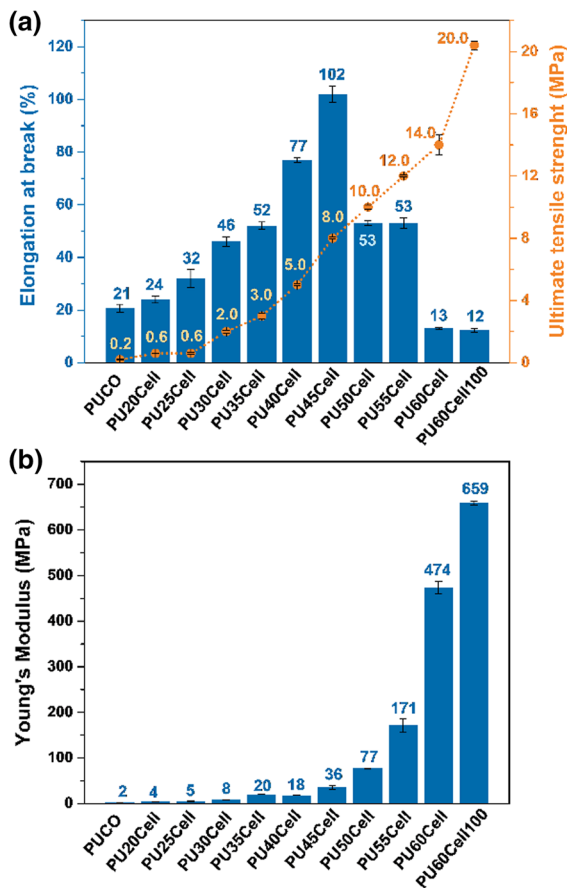
Fig. 11 Tensile strength and elongation at break (**a**), and Young's modulus (**b**) observed for the PUCO, PU20Cell, PU25Cell, PU30Cell, PU35Cell, PU40Cell, PU45Cell, PU50Cell, PU55Cell, PU60Cell, and PU60Cell100 films

The crystallinity is a factor that can contribute to increasing the tensile strength of materials (Trovati et al. 2010). However, similar CrI values (~ 75%) were observed for all of the PU films studied (Table 2), i.e., the crystallinity was not a factor that influenced the tensile strength of the resulting films.

The low values (≤ 3 MPa) observed for the rupture tension from PUCO to PU35Cell can be related to the analyses carried out at room temperature (25 °C), in which these films are above, or close to, their respective T_g (Fig. 10), due to the prevalence of flexible chains originating from the triglyceride of ricinoleic acid present in CO. The mobility of the segments from CO present in the non-crystalline regions may facilitate the sliding of the structures in relation to their neighbors, which was partially restricted when

the percentage of MCC was increased from 0 to 45%. The increase in the tensile strength (Fig. 11) was accompanied by a larger elongation at break. For PU40Cell and PU45Cell, the observed properties indicate a balance between the flexible and rigid structures originating from CO and MCC, respectively, leading to elongation values that stood out against the other films.

The tensile strength increased for films where the glass transition is above room temperature (from PU50Cell, Fig. 10). The resistance to deformation increased considerably, as indicated by the significant increase in Young's modulus (Fig. 11) and the decrease in elongation at break. PU60Cell was distinguished due to its high Young's modulus value (Fig. 11) and low elongation, indicating the significant impact from the structures introduced by the use of MCC as a polyol and the consequent increase in the complexity of the chemical structure.

When comparing PU60Cell and PU60Cell100, it was observed that the tensile strength increases from 14 to 20 MPa, the modulus increases from 474 to 659 MPa, and the elongation remained constant because although the PU60Cell100 film has a greater resistance to rupture, providing in principle greater possibilities of deformation, this did not occur because the resistance to deformation increased (Fig. 11).

Biocompatibility

Figure 12 shows the cell viability observed for PUCO, PU30Cell, PU60Cell, and PU60Cell100. The films were selected for analysis considering the PUCO film (prepared in the absence of MCC as a polyol), the percentage of MCC used from intermediate (PU30Cell) to high (PU60Cell), and the synthesis carried out above room temperature (PU60Cell100), and used as indicators of the cytotoxicity of the PU films studied.

The cytotoxicity of the films was quantitatively evaluated using an MTT assay and compared to the control sample. The cytotoxicity of a material can be classified according to percentage of viable cells: as high (< 30%), moderate (30–60%), mild (60–90%), or non-cytotoxic (> 90%) in relation to the values obtained for the control sample (Dioguardi et al. 2015). For all media, in which the films were kept in contact with cell culture media for 24 to 168 h, and
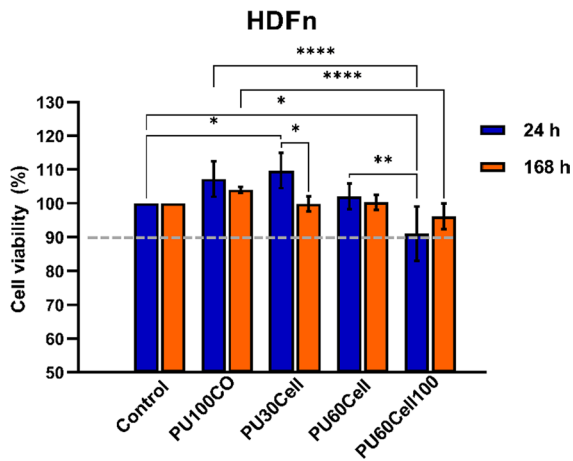
HDFn

Fig. 12 The cell viability determined using an MTT assay observed for the PUCO, PU30Cell, PU60Cell and PU60Cell100 films after 24 h and 168 h upon concentration of the extracts in the samples. Statistical analysis was performed using the two-way ANOVA method with Turkey's comparison. All measurements are presented as the mean $\pm$ SD. *$p < 0.1$; **$p < 0.01$; *HDFn* human fibroblast

incubated for 24 h with HDFn cells, a cell viability of > 90% was observed (Fig. 12), indicating that none of the films exhibited cytotoxicity.

After 24 h, the PUCO, PU30Cell, and PU60Cell films showed values > 100%, indicating a stimulus for cell growth. For the same films, a decrease in the cell viability was observed after 168 h, but with values above or very close to 100%, showing that even after one week, the PUs remained non-cytotoxic. The cytotoxicity of macromolecular materials is usually associated with the presence of degradation products, small molecule impurities, and interactions with macromolecules in intracellular processes and/ or the cell membrane (Khadivi et al. 2019). In the FTIR spectra, the presence of unreacted isocyanates was not observed, which could be characterized as impurities and eventually be toxic to HDFn cells. The small reduction after one week can be related to the interactions of macromolecules in intracellular and/or cell membrane processes that may occur after greater exposure of the cells to the extract in which the films were kept. However, as mentioned above, the films were not cytotoxic.

For PU30Cell, a statistically significant difference was observed ($p < 0.1$) for the values observed after 24 and 168 h, indicating a change in the viability after greater exposure of the cells to the medium in which

the film was kept. Despite this, it is noteworthy that even after 168 h, the PU30Cell film showed good biocompatibility.

The results of the cell viability after 24 h observed for PU30Cell show a statistically significant difference ($p < 0.1$) with the control (absence of PU), as well as for the PUCO film, in which only CO was used as a polyol in the synthesis that generated the film, indicating cell growth with a viability of ~ 110%.

A decrease in viability was observed after 24 h for the PU60Cell and PU60Cell100 films when compared to the control (PUCO) and PU30Cell films, indicating that the greater insertion of MCC structures and consequently, pMDI in the PU structure led to a reduction in cell growth. PU60Cell100 exhibited viability after 24 and 168 h similar to PU60Cell, indicating that the synthesis temperature at 100 °C did not change the biocompatibility of the material with viability (24 and 168 h) close to 100% for both films.

Conclusions

The present study has shown the feasibility of using MCC as a renewable polyol in the synthesis of PUs, from low to high percentages, which can be considered an important expansion in cellulose derivatization. Film formation simultaneously with syntheses was targeted, but it should be highlighted that the strategy used in syntheses can be adapted to other types of products.

The results have shown that important film properties can be tuned by the percentage of cellulose used as a polyol in the synthesis. For example, the glass transition temperature, tensile strength, and Young's modulus increase with an increase in the percentage of MCC used, and the elongation at break decreased. Other properties such as the thermal stability, surface hydrophilicity, and crystallinity were not significantly affected by the variation in the percentage of MCC used in the synthesis of the PUs.

The non-cytotoxicity of the films can be emphasized, as they expand their application possibilities, for example, in dressings. In addition, packaging and coatings can also be mentioned as possible applications, among others. This process does not involve complexity, which favors scale-up.

The approach of this study, which contributes to the advancement of the bioeconomy, is unprecedented, as far as is known.

Declarations

Conflict of intetest The authors declare that they have no conflict of interest.

References

Ahvenainen P, Kontro I, Svedström K (2016) Comparison of sample crystallinity determination methods by X-ray diffraction for challenging cellulose I materials. Cellulose 23:1073–1086. https://doi.org/10.1007/s10570-016-0881-6

Belachew T, Gebino G, Haile A (2021) Extraction and characterization of indigenous Ethiopian castor oil bast fibre. Cellulose 28:2075–2086. https://doi.org/10.1007/s10570-020-03667-9

Cao S, Li S, Li M et al (2017) A thermal self-healing polyurethane thermoset based on phenolic urethane. Polym J 49:775–781. https://doi.org/10.1038/pj.2017.48

Cassales A, Ramos LA, Frollini E (2020) Synthesis of bio-based polyurethanes from Kraft lignin and castor oil with simultaneous film formation. Int J Biol Macromol 145:28–41. https://doi.org/10.1016/j.ijbiomac.2019.12.173

Chen Y-C, Tai W (2018) Castor oil-based polyurethane resin for low-density composites with bamboo charcoal. Polymers (basel) 10:1–12. https://doi.org/10.3390/polym10101100

Crist B, Schultz JM (2016) Polymer spherulites: a critical review. Prog Polym Sci 56:1–63. https://doi.org/10.1016/j.progpolymsci.2015.11.006

da Silva JEE, Alarcon RT, Gaglieri C et al (2018) New thermal study of polymerization and degradation kinetics of methylene diphenyl diisocyanate. J Therm Anal Calorim 133:1455–1462. https://doi.org/10.1007/s10973-018-7211-1

de Oliveira F, Ramires EC, Frollini E, Belgacem MN (2015) Lignopolyurethanic materials based on oxypropylated sodium lignosulfonate and castor oil blends. Ind Crops Prod 72:77–86. https://doi.org/10.1016/j.indcrop.2015.01.023

de Oliveira F, Gonçalves LP, Belgacem MN, Frollini E (2020) Polyurethanes from plant- and fossil-sourced polyols: properties of neat polymers and their sisal composites. Ind Crops Prod 155:112821. https://doi.org/10.1016/j.indcrop.2020.112821

Dioguardi M, Perrone D, Troiano G et al (2015) Cytotoxicity evaluation of five different dual-cured resin cements used for fiber posts cementation. Int J Clin Exp Med 8:9327–9333

Duan C, Long Y, Li J et al (2015) Changes of cellulose accessibility to cellulase due to fiber hornification and its impact on enzymatic viscosity control of dissolving pulp. Cellulose 22:2729–2736. https://doi.org/10.1007/s10570-015-0636-9

Dwivedi C, Pandey I, Pandey H et al (2017) Electrospun nanofibrous scaffold as a potential carrier of antimicrobial therapeutics for diabetic wound healing and tissue regeneration. In: Grumezescu AM (ed) Nano- and microscale drug delivery systems: design and fabrication. Elsevier Inc., Amsterdam, pp 147–164

French AD (2014) Idealized powder diffraction patterns for cellulose polymorphs. Cellulose 21:885–896. https://doi.org/10.1007/s10570-013-0030-4

Ghobashy MM, Abdeen ZI (2016) Radiation crosslinking of polyurethanes: characterization by FTIR, TGA, SEM, XRD, and Raman spectroscopy. J Polym 2016:1–9. https://doi.org/10.1155/2016/9802514

Gómez-Jiménez-Aberasturi O, Ochoa-Gómez JR (2017) New approaches to producing polyols from biomass. J Chem Technol Biotechnol 92:705–711. https://doi.org/10.1002/jctb.5149

Güney A, Hasirci N (2014) Properties and phase segregation of crosslinked PCL-based polyurethanes. J Appl Polym Sci 131:1–13. https://doi.org/10.1002/app.39758

Hamad WY, Miao C, Beck S (2019) Growing the bioeconomy: advances in the development of applications for cellulose filaments and nanocrystals. Ind Biotechnol 15:133–137. https://doi.org/10.1089/ind.2019.29172.qyh

Ikhwan FH, Ilmiati S, Kurnia Adi H et al (2017) Novel route of synthesis for cellulose fiber-based hybrid polyurethane. IOP Conf Ser Mater Sci Eng 223:0–11. https://doi.org/10.1088/1757-899X/223/1/012019

International Organization for Standardization (ISO) (2009) International Organization for Standardization: Tests for in Vitro Cytotoxicity, in ISO 10993-5: Biological Evaluation of Medical Devices. https://www.iso.org/standard/36406.html

Jia Z, Lu C, Zhou P, Wang L (2015) Preparation and characterization of high boiling solvent lignin-based polyurethane film with lignin as the only hydroxyl group provider. RSC Adv 5:53949–53955. https://doi.org/10.1039/c5ra09477a

Kaschuk JJ, Frollini E (2018) Effects of average molar weight, crystallinity, and hemicelluloses content on the enzymatic hydrolysis of sisal pulp, filter paper, and microcrystalline cellulose. Ind Crops Prod 115:280–289. https://doi.org/10.1016/j.indcrop.2018.02.011

Katakojwala R, Mohan SV (2020) Microcrystalline cellulose production from sugarcane bagasse: Sustainable process development and life cycle assessment. J Clean Prod 249:119342. https://doi.org/10.1016/j.jclepro.2019.119342

Khadivi P, Salami-Kalajahi M, Roghani-Mamaqani H (2019) Evaluation of in vitro cytotoxicity and properties of polydimethylsiloxane-based polyurethane/crystalline nanocellulose bionanocomposites. J Biomed Mater Res Part A 107:1771–1778. https://doi.org/10.1002/jbm.a.36696

Khanderay JC, Gite VV (2019) Fully biobased polyester polyols derived from renewable resources toward preparation of polyurethane and their application for coatings. J Appl Polym Sci 136:1–9. https://doi.org/10.1002/app.47558

Kontturi KS, Lee KY, Jones MP et al (2021) Influence of biological origin on the tensile properties of cellulose nanopapers. Cellulose 28:6619–6628. https://doi.org/10.1007/s10570-021-03935-2

Lan Z, Chen X, Zhang X et al (2019) Transparent, high glass-transition temperature, shape memory hybrid polyimides based on polyhedral oligomeric silsesquioxane. Polymers (basel) 11:1–11. https://doi.org/10.3390/POLYM11061058

Liao Y, Cao B, Liu L et al (2021) Structure and properties of bio-based polyurethane coatings for controlled-release fertilizer. J Appl Polym Sci 138:1–7. https://doi.org/10.1002/app.50179

Lin S, Huang J, Chang PR et al (2013) Structure and mechanical properties of new biomass-based nanocomposite: castor oil-based polyurethane reinforced with acetylated cellulose nanocrystal. Carbohydr Polym 95:91–99. https://doi.org/10.1016/j.carbpol.2013.02.023

Lin Y, Li M, Xia J et al (2021) Synthesis of plant oil derived polyols and their effects on the properties of prepared ethyl cellulose composite films. Cellulose. https://doi.org/10.1007/s10570-021-03811-z

Lyu B, Cheng K, Gao D et al (2019) Enhanced hygienic property of solvent-free polyurethane film by hollow TiO$_2$ microspheres. J Clean Prod 209:608–616. https://doi.org/10.1016/j.jclepro.2018.10.282

Marcovich NE, Auad ML, Bellesi NE et al (2006) Cellulose micro/nanocrystals reinforced polyurethane. J Mater Res 21:870–881. https://doi.org/10.1557/jmr.2006.0105

Mathew A, Kurmvanshi S, Mohanty S, Nayak SK (2018) Sustainable production of polyurethane from castor oil, functionalized with epoxy- and hydroxyl-terminated poly(dimethyl siloxane) for biomedical applications. J Mater Sci 53:3119–3130. https://doi.org/10.1007/s10853-017-1757-3

Morsi SMM, Mohamed HA (2017) A comparative study of new linear and hyperbranched polyurethanes built up from a synthesized isocyanate-terminated polyester/urethane. Polym Bull 74:5011–5027. https://doi.org/10.1007/s00289-017-1996-0

Ni H, Liu J, Wang Z, Yang S (2015) A review on colorless and optically transparent polyimide films: chemistry, process and engineering applications. J Ind Eng Chem 28:16–27. https://doi.org/10.1016/j.jiec.2015.03.013

Noreen A, Zia KM, Zuber M et al (2016) Bio-based polyurethane: an efficient and environment friendly coating systems: a review. Prog Org Coat 91:25–32. https://doi.org/10.1016/j.porgcoat.2015.11.018

Ramires EC, Megiatto JD, Dufresne A, Frollini E (2020) Cellulose nanocrystals versus microcrystalline cellulose as reinforcement of lignopolyurethane matrix. Fibers. https://doi.org/10.3390/fib8040021

Reghunadhan A, Thomas S (2017) Polyurethanes: structure, properties, synthesis, characterization, and applications. In: Thomas S, Haponiuk JT, Datta J (eds) Polyurethane polymers: blends and interpenetrating polymer networks. Elsevier, New York, pp 1–16

Rodrigues BVM, Ramires EC, Santos RPO, Frollini E (2015) Ultrathin and nanofibers via room temperature electrospinning from trifluoroacetic acid solutions of untreated lignocellulosic sisal fiber or sisal pulp. J Appl Polym Sci 132:1–8. https://doi.org/10.1002/app.41826

Sawpan MA (2018) Polyurethanes from vegetable oils and applications: a review. J Polym Res. https://doi.org/10.1007/s10965-018-1578-3

Scheirs J, Camino G, Tumiatti W (2001) Overview of water evolution during the thermal degradation of cellulose. Eur Polym J 37:933–942. https://doi.org/10.1016/S0014-3057(00)00211-1

Seddiqi H, Oliaei E, Honarkar H et al (2021) Cellulose and its derivatives: towards biomedical applications. Cellulose 28:1893–1931. https://doi.org/10.1007/s10570-020-03674-w

Sjahro N, Yunus R, Abdullah LC et al (2021) Recent advances in the application of cellulose derivatives for removal of contaminants from aquatic environments. Cellulose. https://doi.org/10.1007/s10570-021-03985-6

Skoog DA, Holler FJ, Crouch SR (2014) Principles of instrumental analysis, 6th edition. Cengage Learning, Boston

Solanki A, Thakore S (2015) Cellulose crosslinked pH-responsive polyurethanes for drug delivery: α-hydroxy acids as drug release modifiers. Int J Biol Macromol 80:683–691. https://doi.org/10.1016/j.ijbiomac.2015.07.003

Su Q, Wei D, Dai W et al (2019) Designing a castor oil-based polyurethane as bioadhesive. Colloids Surf B Biointerfaces 181:740–748. https://doi.org/10.1016/j.colsurfb.2019.06.032

TAPPI (2008) TAPPI Useful Method. T230 om-08: Viscosity of pulp (capillary viscometer method). Atlanta, GA, USA

Tolbert A, Akinosho H, Khunsupat R (2014) Characterization and analysis of the molecular weight of lignin for biorefining studies. Biofuels Bioprod Biorefin 8:836–856. https://doi.org/10.1002/bbb.1500

Trovati G, Sanches EA, Neto S, c, et al (2010) Characterization of polyurethane resins by FTIR, TGA, and XRD. J Appl Polym Sci 116:2658–2667. https://doi.org/10.1002/app

Turan D (2021) Water vapor transport properties of polyurethane films for packaging of respiring foods. Food Eng Rev 13:54–65. https://doi.org/10.1007/s12393-019-09205-z

Urbina L, Alonso-Varona A, Saralegi A et al (2019) Hybrid and biocompatible cellulose/polyurethane nanocomposites with water-activated shape memory properties. Carbohydr Polym 216:86–96. https://doi.org/10.1016/j.carbpol.2019.04.010

Villegas-Villalobos S, Díaz LE, Vilariño-Feltrer G et al (2018) Effect of an organotin catalyst on the physicochemical properties and biocompatibility of castor oil-based polyurethane/cellulose composites. J Mater Res 33:2598–2611. https://doi.org/10.1557/jmr.2018.286

Wang X, Zhang Y, Liang H et al (2019) Synthesis and properties of castor oil-based waterborne polyurethane/sodium alginate composites with tunable properties. Carbohydr Polym 208:391–397. https://doi.org/10.1016/j.carbpol.2018.12.090

Wong CS, Badri KH (2012) Chemical analyses of palm kernel oil-based polyurethane prepolymer. Mater Sci Appl 03:78–86. https://doi.org/10.4236/msa.2012.32012

Wong A, Santos AM, Baccarin M et al (2019) Simultaneous determination of environmental contaminants using a graphite oxide—polyurethane composite electrode modified with cyclodextrin. Mater Sci Eng C 99:1415–1423. https://doi.org/10.1016/j.msec.2019.02.093

Yanagihara Y, Suenaga A, Kondo H, Saito H (2017) Structure and deformation recovery of the thermoplastic polyurethane spherulite. J Polym Sci Part B Polym Phys 55:1585–1594. https://doi.org/10.1002/polb.24412

Yuwawech K, Woothikanokkhan J, Wanwong S, Tanpichai S (2017) Green and sustainable polyurethanes for advanced applications. J Appl Polym Sci. https://doi.org/10.1002/app.45646

Zhang J, Tang Y-F, Liu J, Chen Y (2014) Thermal stability and thermal degradaton reaction kinetics of 4,4'-diphenylmethane diisocyanatetrimer. Asian J Chem 26:6073–6076. https://doi.org/10.14233/ajchem.2014.17278

Zheng Y, Fu Z, Li D, Wu M (2018) Effects of ball milling processes on the microstructure and rheological properties of microcrystalline cellulose as a sustainable polymer additive. Materials (basel) 11:1–13. https://doi.org/10.3390/ma11071057

Zugenmaier P (2008) Crystalline cellulose and cellulose derivatives, 1st edn. Springer, New York